Article

Integrated turnkey soliton microcombs

https://doi.org/10.1038/s41586-020-2358-x

Received: 22 November 2019

Accepted: 23 March 2020

Published online: 17 June 2020

Check for updates

Boqiang Shen[1,6], Lin Chang[2,6]✉, Junqiu Liu[3,6], Heming Wang[1,6], Qi-Fan Yang[1,6], Chao Xiang[2], Rui Ning Wang[3], Jijun He[3], Tianyi Liu[3], Weiqiang Xie[2], Joel Guo[2], David Kinghorn[2,4], Lue Wu[1], Qing-Xin Ji[1,5], Tobias J. Kippenberg[3]✉, Kerry Vahala[1]✉ & John E. Bowers[2]

Optical frequency combs have a wide range of applications in science and technology[1]. An important development for miniature and integrated comb systems is the formation of dissipative Kerr solitons in coherently pumped high-quality-factor optical microresonators[2–9]. Such soliton microcombs[10] have been applied to spectroscopy[11–13], the search for exoplanets[14,15], optical frequency synthesis[16], time keeping[17] and other areas[10]. In addition, the recent integration of microresonators with lasers has revealed the viability of fully chip-based soliton microcombs[18,19]. However, the operation of microcombs requires complex startup and feedback protocols that necessitate difficult-to-integrate optical and electrical components, and microcombs operating at rates that are compatible with electronic circuits—as is required in nearly all comb systems—have not yet been integrated with pump lasers because of their high power requirements. Here we experimentally demonstrate and theoretically describe a turnkey operation regime for soliton microcombs co-integrated with a pump laser. We show the appearance of an operating point at which solitons are immediately generated by turning the pump laser on, thereby eliminating the need for photonic and electronic control circuitry. These features are combined with high-quality-factor Si_3N_4 resonators to provide microcombs with repetition frequencies as low as 15 gigahertz that are fully integrated into an industry standard (butterfly) package, thereby offering compelling advantages for high-volume production.

The integration of microcomb systems faces two considerable obstacles. First, complex tuning schemes and feedback loops are required for the generation and stabilization of solitons[2,20,21]. These not only introduce redundant and power-hungry electronic components[18,19], but also require optical isolation, which has so far been challenging to integrate at acceptable performance levels. Second, repetition frequencies that are both detectable and readily processed by integrated electronic circuits, such as complementary metal–oxide–semiconductor (CMOS) circuits, are essential for comb self-referencing, the key process that underlies many comb applications[1]. Although silica resonators[5,22] and Damascene Si_3N_4 resonators[23] with ultrahigh quality factors (Q) can attain these rates, their integration with pump lasers has not been possible. Here we show that the nonlinear dynamics of an unisolated laser–microcomb system creates an operating point at which the soliton mode-locking process is initiated by simply turning on the pump laser. We demonstrate the existence and substantial benefits of this turnkey operating point theoretically and experimentally. The resulting microcomb system has a Q factor that enables operation at electronic-circuit rates using an integrated pump laser.

In the experiment, integrated soliton microcombs with CMOS-compatible[24] fabrication and repetition rates (40 GHz down to 15 GHz) are butt-coupled to a commercial distributed-feedback (DFB) laser via inverse tapers (Fig. 1a). The microresonators are fabricated using the photonic Damascene reflow process[23,25] and feature Q factors exceeding 16×10^6 (Fig. 1b), resulting in a low, milliwatt-level parametric oscillation threshold, despite the larger mode volumes required by gigahertz-rate microcombs compared with those of microcombs operating at hundreds of gigahertz. This enables chip-to-chip pumping of the microcombs at such challenging repetition rates. Optical power of up to 30 mW is launched into the microresonator. Feedback from the resonator suppresses the frequency noise by around 30 dB compared with that of a free-running DFB laser (Fig. 1c) so that the laser noise performance surpasses state-of-the-art monolithically integrated lasers[26] and table-top external-cavity diode lasers (ECDLs). Given its compact footprint and the absence of control electronics, the pump laser–microcomb chipset is mounted into a butterfly package (Fig. 1d) to facilitate measurements and enable portability. This level of integration and packaging, combined with turnkey operation, makes this a completely functional device suitable for use at any system level.

In conventional pumping of microcombs, the laser is optically isolated from the downstream optical path so as to prevent feedback-induced interference (Fig. 2a). Because of strong high-Q-induced resonant build-up and the Kerr nonlinearity, the intracavity power as a function of pump–cavity detuning features bistability. The resulting dynamics can be described using a phase diagram comprising continuous-wave, modulation-instability (MI) combs and soliton regimes that are accessed as the pump frequency is tuned across a cavity resonance. A typical plot versus the frequency difference $\delta\omega$ between the cavity

[1]T. J. Watson Laboratory of Applied Physics, California Institute of Technology, Pasadena, CA, USA. [2]ECE Department, University of California Santa Barbara, Santa Barbara, CA, USA. [3]Institute of Physics, Swiss Federal Institute of Technology Lausanne (EPFL), Lausanne, Switzerland. [4]Pro Precision Process and Reliability LLC, Carpinteria, CA, USA. [5]School of Physics, Peking University, Beijing, China. [6]These authors contributed equally: Boqiang Shen, Lin Chang, Junqiu Liu, Heming Wang, Qi-Fan Yang. ✉e-mail: linchang@ucsb.edu; tobias.kippenberg@epfl.ch; vahala@caltech.edu

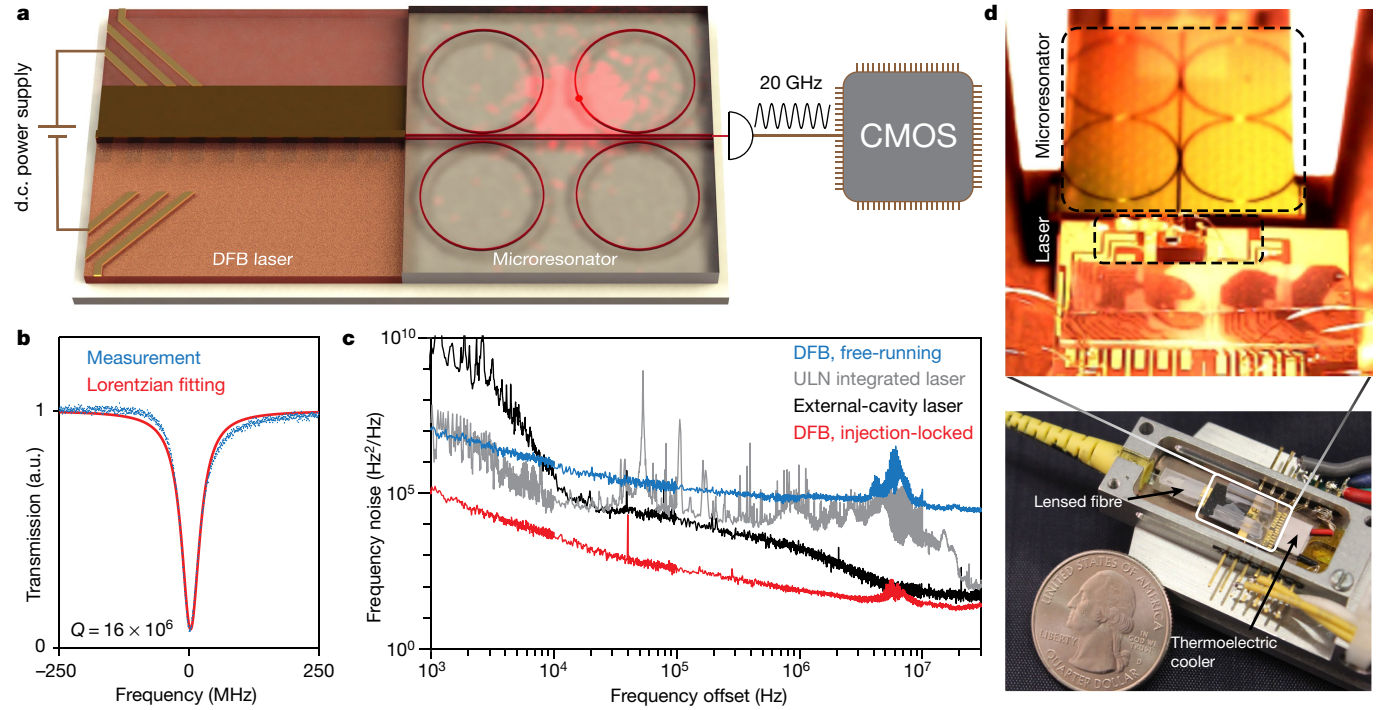

Fig. 1 | Integrated soliton microcomb chip. a, A soliton microcomb chip driven by a d.c. power source produces soliton pulse signals at electronic-circuit rates. Four microcombs are integrated on one chip, but only one is used in these measurements. **b**, Transmission signal obtained when scanning the laser across a cavity resonance (blue). A Lorentzian fitting (red) gives an intrinsic Q factor of 16×10^6. a.u., arbitrary units. **c**, Frequency noise spectral densities of the DFB laser when it is free-running (blue) and feedback-locked to a high-Q Si_3N_4 microresonator (red). For comparison, the frequency noise spectral densities of an ultralow-noise (ULN) integrated laser on silicon (grey) and a table-top external-cavity diode laser (black) are also plotted. **d**, Images of a pump–microcomb system in a compact butterfly package.

resonance and the pump laser (that is, $\delta\omega > 0$ indicates red detuning of the pump frequency relative to the cavity frequency)[2] is shown in Fig. 2b. Tuning through the MI regime seeds the formation of soliton pulses. Because of the thermal hysteresis[27] and the abrupt intracavity power discontinuity upon transition to the soliton regime (Fig. 2c), delicate tuning waveforms[2,21] or active capturing techniques[20] are essential to compensate for the thermal transients, except in materials with effectively negative thermo-optic response[8].

Now we consider removing the optical isolation, as shown in Fig. 2d, to enable backscatter feedback from pumping a resonator mode. In previous work, semiconductor laser locking to the resonator mode and laser line narrowing have been shown to result from backscattering of the intracavity optical field[28]. These attributes, as well as mode selection when using a broadband pump, have also been advantageously applied to operate microcomb systems without isolation[18,19,29,30]. However, these previous studies of feedback effects considered the resonator to be linear so that the detuning between the feedback-locked laser and the cavity resonance was determined solely by the phase ϕ accumulated in the feedback path[31]. By contrast, here the nonlinear behaviour of the microresonator is included, and it is shown to have a dramatic effect on the operating point of the system. In addition, the nonlinear behaviour causes the resonances to be red-shifted by intensity-dependent self- and cross-phase modulation. As a result, the relationship between frequency detuning and intracavity power of the pump mode P_0 can be shown (see Supplementary Information) to be approximately given by

$$\frac{\delta\omega}{\kappa/2} = \tan\frac{\phi}{2} + \frac{3}{2}\frac{P_0}{P_{th}} \quad (1)$$

where κ is the power decay rate of the resonance and P_{th} is the parametric oscillation threshold for intracavity power. This dependence of detuning on the intracavity power gives rise to a single operating point at the intersection of equation (1) and the hysteresis, as shown in Fig. 2e. Control of the feedback phase shifts the x intercept of equation (1) and thereby adjusts the operating point.

In Supplementary Information it is shown that the system converges to this operating point once the laser frequency is within a locking bandwidth (estimated to be 5 GHz in this case). As verified both numerically (Fig. 2e) and experimentally (Fig. 2f), this behaviour enables soliton mode-locking by simply powering on the pump laser (that is, without any triggering or complex tuning schemes). A simulated trajectory is shown in Fig. 2e, where a laser is initially started to the red of the high-Q cavity resonance frequency and well outside its linewidth. The system is attracted towards the resonance through a process that at first resembles injection locking of the III–V laser. However, as the laser frequency moves towards the resonance frequency, the resonator power rises and the Kerr nonlinearity induces evolution towards the operating point. The system transiently exceeds the threshold for parametric oscillation and, as shown in Supplementary Information, Turing rolls form, which ultimately evolve into solitons as the system achieves a steady state. An experimental trace of the comb power shows that a steady soliton power plateau is reached immediately after turning on the laser. The stable soliton emission is further confirmed by monitoring the real-time evolution of the soliton repetition rate signal (Fig. 2f). Numerical simulation of this startup process is provided in Supplementary Information and the Supplementary videos. The turnkey operation demonstrated here is automatic, such that the entire soliton initiation and stabilization is described and realized by the physical dynamics of laser self-injection locking in combination with the nonlinear resonator response. Consistent with this point, the system is observed to be highly robust with respect to temperature and environmental disturbances. Indeed, soliton generation without any external feedback control was possible for several hours in the laboratory.

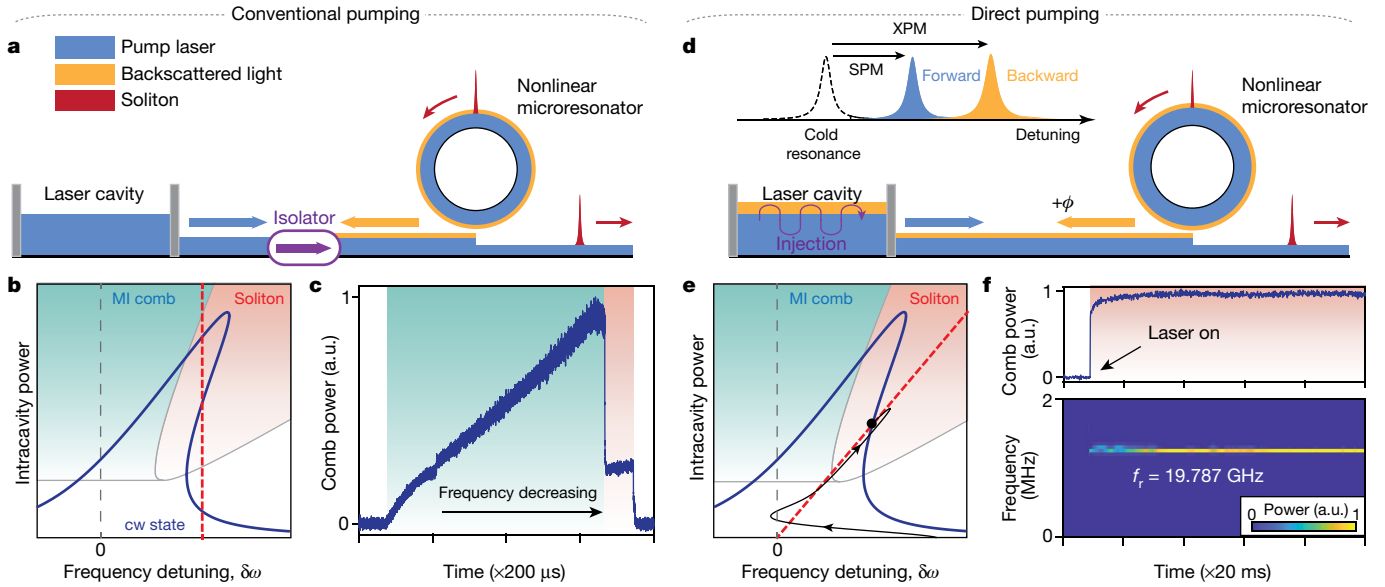

Fig. 2 | The turnkey operating point. a, Operation of a conventional soliton microcomb using a tunable continuous-wave (cw) laser. Pump laser light (blue arrow) is controlled to trigger and stabilize the soliton generation process. An optical isolator blocks the backscattered light (yellow arrow) from the microresonator so that the pump operation is decoupled from the soliton formation. **b**, Phase diagram, hysteresis curve and dynamics of a microresonator pumped as shown in **a**. The blue curve shows the intracavity power as a function of cavity–pump frequency detuning. Laser tuning (dashed red line) accesses multiple equilibria. **c**, Measured evolution of comb power pumped by an isolated, frequency-scanned ECDL. The step in the trace is a characteristic feature of soliton formation. **d**, Turnkey soliton microcomb generation. Non-isolated operation allows backscattered light to be injected into the pump laser cavity. Resonances are red-shifted owing to self-phase modulation (SPM) and cross-phase modulation (XPM). **e**, Phase diagram, hysteresis curve and dynamics of a pump–microresonator system. A modified laser tuning curve (dashed red line) intersects the intracavity power curve (blue) to establish a new operating point at which solitons form. The feedback phase ϕ is set to 0 in the plot. The solid black curve shows the simulated evolution upon turning on the laser at a red detuning outside the soliton regime but within the locking bandwidth. **f**, Measured comb power (top) and detected soliton repetition rate (f_r) signal (bottom) with the laser turn-on indicated at 10 ms.

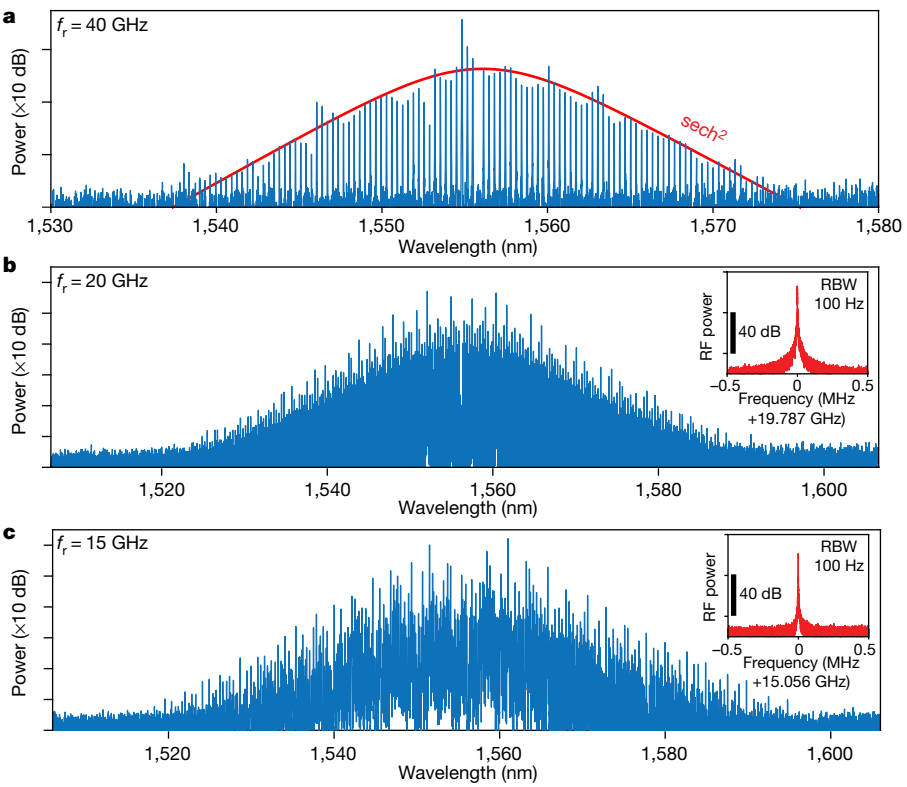

Fig. 3 | Optical and electrical spectra of solitons. a, Optical spectrum of a single soliton state with repetition rate f_r = 40 GHz. The red curve shows a sech^2 fitting to the soliton spectral envelope. **b**, **c**, Optical spectra of multi-soliton states at 20 GHz (**b**) and 15 GHz (**c**) repetition rates. Insets, electrical beatnotes showing the repetition rates. RF, radiofrequency; RBW, resolution bandwidth.

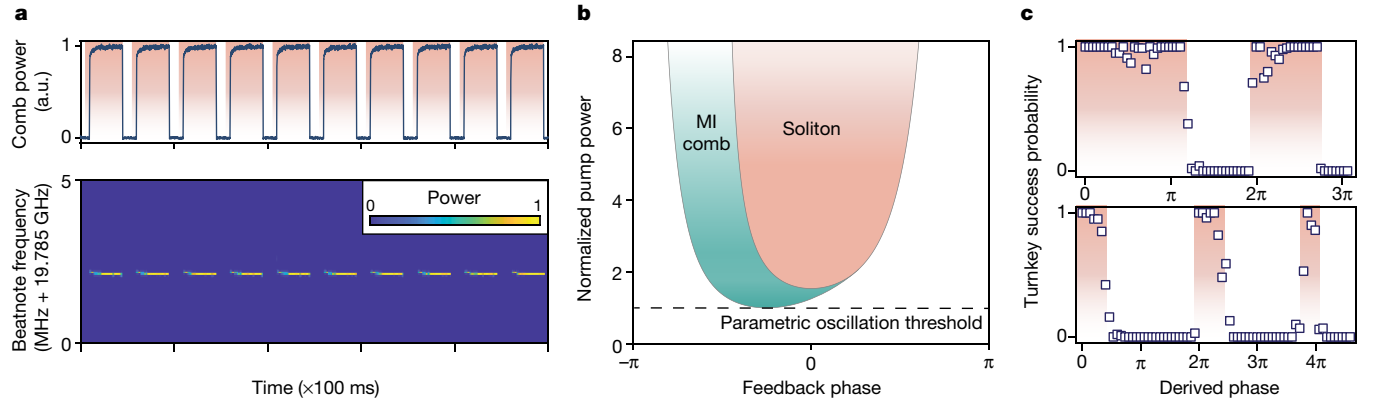

Fig. 4 | Turnkey soliton generation. a, Ten consecutive switching tests are shown. The top panel shows the measured comb power versus time. The laser is switched on periodically, as indicated by the shaded regions. The bottom panel is a spectrogram of the soliton repetition rate signal measured during the switching process. **b**, Phase diagram of the integrated soliton system with respect to the feedback phase and pump power. The pump power is normalized to the parametric oscillation threshold. **c**, Turnkey success probability versus relative feedback phase of devices operating at 20 GHz (top) and 15 GHz (bottom). Each data point is acquired from 100 switch-on attempts. See Methods for additional discussion.

Figure 3 shows the optical spectra of a single-soliton state with a repetition rate of 40 GHz and multi-soliton states with repetition rates of 20 GHz and 15 GHz. The deviation from the theoretical curve (a sech^2 function of the spectral envelope amplitude) is believed to result from a combination of mode-crossing-induced dispersion and the dispersion of the waveguide–resonator coupling strength. The pump laser at 1,556 nm is attenuated at the output by a fibre Bragg grating notch filter in these measurements. The coherent nature of these soliton microcombs is confirmed by photodetection of the soliton pulse streams, and reveals high-contrast, single-tone electrical signals at the indicated repetition rates. Numerical simulations confirm the observed tendency of turnkey soliton states consisting of multiple solitons, which is a direct consequence of the high intracavity power and its associated MI gain dynamics (see Supplementary Information for details). However, single-soliton operation is accessible for a certain combination of pump power and feedback phase.

To demonstrate repeatable turnkey operation, the laser current is modulated to a preset value by a square wave to simulate the turn-on process. Soliton microcomb operation is reliably achieved, as confirmed by monitoring the soliton power and the single-tone beating signal (Fig. 4a). Further insight into the nature of the turnkey operation is provided by the phase diagram near the equilibrium point for different feedback phases and pump powers (Fig. 4b). The turnkey regime occurs above a threshold power within a specific range of feedback phases. Moreover, the regime recurs at 2π increments of the feedback phase, as verified experimentally (Fig. 4c). Consistent with the phase diagram, a binary-like behaviour is observed in the turnkey success probability as the feedback phase is varied. In the measurement, the feedback phase is adjusted by controlling the gap between the facets of the laser and the microcomb bus waveguide. A narrowing of the turnkey success probability window with an increased feedback phase is believed to result from the reduction of the pump power in the bus waveguide with increasing tuning gap (consistent with Fig. 4b).

Besides the physical significance and practical impact of the new operating point, our demonstration of a turnkey operating regime is an important simplification of soliton microcomb systems. Moreover, the application of this method in an integrated CMOS-compatible system represents a milestone towards mass production of optical frequency combs. The butterfly-packaged devices will benefit several comb applications, including miniaturized frequency synthesizers[16] and optical clocks[17]. In such applications, their CMOS rates not only enable integration of electrical control and processing functions, but also provide simple detection and processing of the comb pulses (that is, without the need for millimetre-wave frequency mixers). Moreover, the recent demonstration of low-power comb formation in III–V microresonators[32] suggests that monolithic integration of pumps and soliton microcombs is feasible using the methods developed here. A phase section could be included therein, or in advanced versions of the current approach, to electronically control the feedback phase. The ability to create a complete system including a pump laser without optical isolation is also important. Even in cases in which solitons are pumped using amplification, such as in laser cavity solitons[9], full integration would require difficult-to-integrate optical isolators. It is also important to note that the proposed turnkey approach is a soliton-forming comb, whereas a recent work reported non-soliton Kerr combs[33]. Finally, owing to its simplicity, this approach could be applied in other integrated high-Q microresonator platforms[7,8,22] to attain soliton microcombs across a wide range of wavelengths.

Online content

Any methods, additional references, Nature Research reporting summaries, source data, extended data, supplementary information, acknowledgements, peer review information; details of author contributions and competing interests; and statements of data and code availability are available at https://doi.org/10.1038/s41586-020-2358-x.

1. Diddams, S. A. The evolving optical frequency comb. *J. Opt. Soc. Am. B* **27**, B51–B62 (2010).
2. Herr, T. et al. Temporal solitons in optical microresonators. *Nat. Photon.* **8**, 145–152 (2014).
3. Xue, X. et al. Mode-locked dark pulse Kerr combs in normal-dispersion microresonators. *Nat. Photon.* **9**, 594–600 (2015).
4. Brasch, V. et al. Photonic chip–based optical frequency comb using soliton Cherenkov radiation. *Science* **351**, 357–360 (2016).
5. Yi, X., Yang, Q.-F., Yang, K. Y., Suh, M.-G. & Vahala, K. Soliton frequency comb at microwave rates in a high-Q silica microresonator. *Optica* **2**, 1078–1085 (2015).
6. Obrzud, E., Lecomte, S. & Herr, T. Temporal solitons in microresonators driven by optical pulses. *Nat. Photon.* **11**, 600–607 (2017).
7. Gong, Z. et al. High-fidelity cavity soliton generation in crystalline AlN micro-ring resonators. *Opt. Lett.* **43**, 4366–4369 (2018).
8. He, Y. et al. Self-starting bi-chromatic $LiNbO_3$ soliton microcomb. *Optica* **6**, 1138–1144 (2019).
9. Bao, H. et al. Laser cavity-soliton microcombs. *Nat. Photon.* **13**, 384–389 (2019).
10. Kippenberg, T. J., Gaeta, A. L., Lipson, M. & Gorodetsky, M. L. Dissipative Kerr solitons in optical microresonators. *Science* **361**, eaan8083 (2018).
11. Suh, M.-G., Yang, Q.-F., Yang, K. Y., Yi, X. & Vahala, K. J. Microresonator soliton dual-comb spectroscopy. *Science* **354**, 600–603 (2016).
12. Dutt, A. et al. On-chip dual-comb source for spectroscopy. *Sci. Adv.* **4**, e1701858 (2018).
13. Yang, Q.-F. et al. Vernier spectrometer using counterpropagating soliton microcombs. *Science* **363**, 965–968 (2019).

14. Suh, M.-G. et al. Searching for exoplanets using a microresonator astrocomb. *Nat. Photon.* **13**, 25–30 (2019).
15. Obrzud, E. et al. A microphotonic astrocomb. *Nat. Photon.* **13**, 31–35 (2019).
16. Spencer, D. T. et al. An optical-frequency synthesizer using integrated photonics. *Nature* **557**, 81–85 (2018).
17. Newman, Z. L. et al. Architecture for the photonic integration of an optical atomic clock. *Optica* **6**, 680–685 (2019).
18. Stern, B., Ji, X., Okawachi, Y., Gaeta, A. L. & Lipson, M. Battery-operated integrated frequency comb generator. *Nature* **562**, 401–405 (2018).
19. Raja, A. S. et al. Electrically pumped photonic integrated soliton microcomb. *Nat. Commun.* **10**, 680 (2019); correction **10**, 1623 (2019).
20. Yi, X., Yang, Q.-F., Youl, K. & Vahala, K. Active capture and stabilization of temporal solitons in microresonators. *Opt. Lett.* **41**, 2037–2040 (2016).
21. Joshi, C. et al. Thermally controlled comb generation and soliton modelocking in microresonators. *Opt. Lett.* **41**, 2565–2568 (2016).
22. Yang, K. Y. et al. Bridging ultrahigh-*Q* devices and photonic circuits. *Nat. Photon.* **12**, 297–302 (2018).
23. Liu, J. et al. Ultralow-power chip-based soliton microcombs for photonic integration. *Optica* **5**, 1347–1353 (2018).
24. Abidi, A. A. CMOS microwave and millimeter-wave ICs: the historical background. In *2014 IEEE Int. Symp. Radio-Frequency Integration Technology* http://doi.org/10.1109/RFIT.2014.6933267 (IEEE, 2014).
25. Liu, J. et al. Photonic microwave generation in the X- and K-band using integrated soliton microcombs. *Nat. Photon.* https://doi.org/10.1038/s41566-020-0617-x (2020).
26. Huang, D. et al. High-power sub-kHz linewidth lasers fully integrated on silicon. *Optica* **6**, 745–752 (2019).
27. Carmon, T., Yang, L. & Vahala, K. Dynamical thermal behavior and thermal self-stability of microcavities. *Opt. Express* **12**, 4742–4750 (2004).
28. Liang, W. et al. Whispering-gallery-mode-resonator-based ultranarrow linewidth external-cavity semiconductor laser. *Opt. Lett.* **35**, 2822–2824 (2010).
29. Liang, W. et al. High spectral purity Kerr frequency comb radio frequency photonic oscillator. *Nat. Commun.* **6**, 7957 (2015).
30. Pavlov, N. et al. Narrow-linewidth lasing and soliton Kerr microcombs with ordinary laser diodes. *Nat. Photon.* **12**, 694–698 (2018).
31. Kondratiev, N. et al. Self-injection locking of a laser diode to a high-*Q* WGM microresonator. *Opt. Express* **25**, 28167–28178 (2017).
32. Chang, L. et al. Ultra-efficient frequency comb generation in AlGaAs-on-insulator microresonators. *Nat. Commun.* **11**, 1331 (2020).
33. Kim, B. Y. et al. Turn-key, high-efficiency Kerr comb source. *Opt. Lett.* **44**, 4475–4478 (2019).

Methods

Silicon nitride chip fabrication

The Si_3N_4 (ref. [34]) chip devices were fabricated using the photonic Damascene reflow process[35]. Deep-ultraviolet stepper lithography was used to pattern the waveguides and the stress-release patterns[35] to prevent cracks in the Si_3N_4 film from the low-pressure chemical vapour deposition (LPCVD) process. The waveguide patterns were dry-etched into the SiO_2 substrate using a photoresist mask. The substrate was then annealed at 1,250 °C at atmospheric pressure so that SiO_2 reflow occurred, which reduced the waveguide sidewall roughness[36]. Afterwards, Si_3N_4 was deposited on the substrate by LPCVD, followed by chemical–mechanical polishing to planarize the substrate top surface. The substrate was further annealed to remove residual hydrogen in Si_3N_4, followed by deposition of a thick SiO_2 top cladding and annealing of the SiO_2.

To separate the wafer into chips of 5×5 mm^2, deep reactive ion etching (RIE) was used to define the chip facets for superior surface quality, which was particularly important for achieving good contact for the butt-coupling between the Si_3N_4 chip and the laser chip. Typically, dicing of SiO_2 and silicon together is used; however, this method does not easily achieve smooth SiO_2 facets owing to the very narrow operational window of SiO_2 dicing. In our fabrication process, AZ 9260 photoresist of 8 μm thickness was used as the mask for the deep RIE to create the chip facets. The RIE was composed of two steps: dry etching of 7-μm-thick SiO_2 using $He/H_2/C_4F_8$ etchants and a Bosch process to remove the 200-μm-thick silicon using SF_6/C_4F_8 etchants. The deep RIE can thus create a smooth chip facet for butt-coupling, as shown in Extended Data Fig. 1b. After the deep RIE, the wafer was diced into chips using only the silicon dicing recipe.

DFB laser characterization

The DFB pump laser (Freedom Photonics[37]) has high-reflection coatings on the back facet and anti-reflection coatings on the front facet. The threshold current is 50 mA, and the total output power of the laser can reach 125 mW with a slope efficiency of around 0.28 mW mA^{-1} (see Extended Data Fig. 1d). The peak wall-plug efficiency is inferred to be approximately 20%. This power level, combined with the substantially reduced loss in the microresonator (high Q), enables soliton operation using an integrated pump at a low repetition rate that was not attainable in previous work[19]. The lasing is single-mode and its wavelength also shifts from ~1,554.5 nm to ~1,556.5 nm with increasing bias current (about −1.4 GHz mA^{-1}). The temperature of the laser diode can be controlled within 1 mK.

Experimental details

The laser frequency noise is obtained using an OEWaves optical frequency noise analyser. A table-top ECDL (81608A, Keysight) is used for the frequency noise measurement in Fig. 1c. The soliton beatnote is detected by an external fibre-coupled fast photodetector and down-mixed with a local oscillator to measure its real-time evolution. The frequency of the local oscillator is set slightly lower than the repetition rate of the solitons. A high-speed oscilloscope is used to record the trace from which the power spectrum is obtained by fast Fourier transform. The time window of the spectrograph is 20 μs and the resolution bandwidth is 50 kHz.

The relative feedback phases are estimated from the gap between the facets of the laser and the bus waveguide, which can be adjusted by an open-loop piezo micro-stepping motor (PZA12, Newport). The step size of the actuator is calibrated to be 4.3 ± 0.2 nm using the reference mark on the chip. The derived phase has a relative uncertainty of 4%.

During the experiment, the direct reflection from the smooth resonator chip interface sometimes could cause the laser to operate multi-mode and hamper self-injection to the resonance. To counteract this effect, the laser was tilted vertically 3° to 5° relative to the microcomb chip in order to steer the reflection beam spot away from the laser waveguide. The facet-coupling loss was estimated to be close to 3–5 dB by monitoring the total non-resonant transmission through the waveguide. Discussion of facet reflection and waveguide backscatter is provided in Supplementary Information.

Data availability

The data that support the findings of this study are available from the corresponding authors upon reasonable request.

Code availability

The code used in this study is available from the corresponding authors upon reasonable request.

34. Moss, D. J., Morandotti, R., Gaeta, A. L. & Lipson, M. New CMOS-compatible platforms based on silicon nitride and Hydex for nonlinear optics. *Nat. Photon.* **7**, 597–607 (2013).
35. Pfeiffer, M. H. P. et al. Photonic Damascene process for low-loss, high-confinement silicon nitride waveguides. *IEEE J. Sel. Top. Quantum Electron.* **24**, 1–11 (2018).
36. Pfeiffer, M. H. P. et al. Ultra-smooth silicon nitride waveguides based on the Damascene reflow process: fabrication and loss origins. *Optica* **5**, 884–892 (2018).
37. Mashanovitch, M. et al. High-power, efficient DFB laser technology for RF photonics links. In *IEEE Avionics and Vehicle Fiber-Optics and Photonics Conf.*, 17–18 (IEEE, 2018).

Acknowledgements We thank G. Keeler, S. Papp, T. Briles, J. Norman and M. Tran for discussions, Y. Tong and S. Liu for assistance in characterizations, and Freedom Photonics for providing the lasers. The Si_3N_4 microresonators were fabricated at the EPFL Center of MicroNanoTechnology (CMi). This work is supported by the Defense Advanced Research Projects Agency (DARPA) under DODOS (HR0011-15-C-055) programmes of the Microsystems Technology Office (MTO).

Author contributions B.S., L.C., Q.-F.Y., J.L., T.J.K., J.E.B. and K.V. conceived the experiment. D.K., L.C., B.S. and Q.-F.Y. packaged the chip. J.L., R.N.W., J.H. and T.L. designed, fabricated and tested the Si_3N_4 chip devices. H.W. constructed the theoretical model. Measurements were performed by B.S., L.C. and Q.-F.Y. with assistance from H.W., C.X., W.X., J.G., L.W. and Q.-X.J. All authors analysed the data and contributed to writing the manuscript. J.E.B., K.V. and T.J.K. supervised the project and the collaboration.

Competing interests The authors declare no competing interests.

Additional information
Supplementary information is available for this paper at https://doi.org/10.1038/s41586-020-2358-x.
Correspondence and requests for materials should be addressed to L.C., T.J.K. or K.V.
Peer review information *Nature* thanks Luigi Lugiato and the other, anonymous, reviewer(s) for their contribution to the peer review of this work.
Reprints and permissions information is available at http://www.nature.com/reprints.

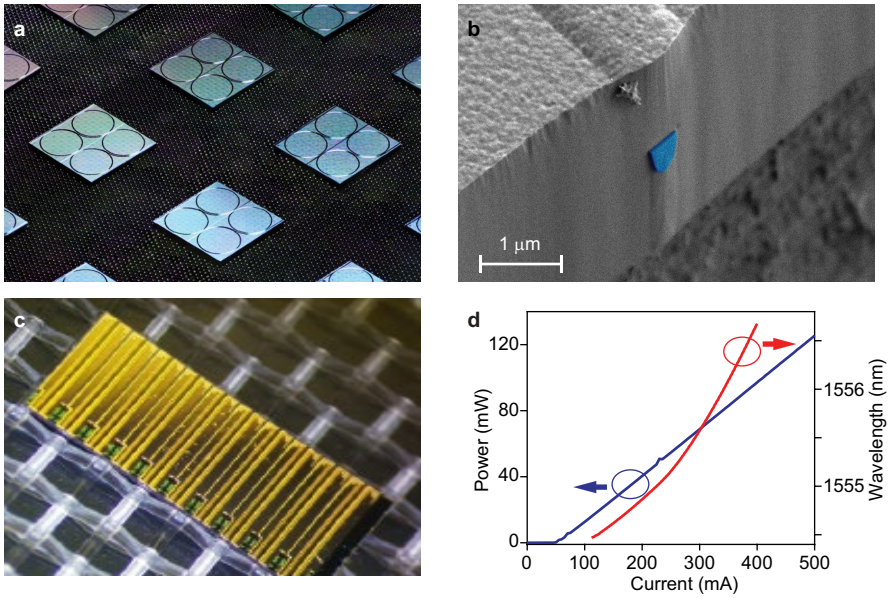

Extended Data Fig. 1 | Images and characteristics of microcomb resonators and pump lasers. a, Photograph of Si_3N_4 microresonator chip devices. **b**, Scanning electron microscope image of the smooth facet of a Si_3N_4 chip. The Si_3N_4 inverse taper for butt-coupling is shown in blue. **c**, Microscopic image of a chip with ten DFB lasers. **d**, Light–current curve (blue; left vertical axis) and the wavelength response (red; right vertical axis) of the DFB laser.